nature photonics
SUPPLEMENTARY INFORMATION
DOI: 10.1038/NPHOTON.2014.213

Mid-infrared supercontinuum covering the 1.4–13.3 μm molecular fingerprint region using ultra-high NA chalcogenide step-index fibre

Christian Rosenberg Petersen*[1], Uffe Møller[1], Irnis Kubat[1], Binbin Zhou[1], Sune Dupont[2], Jacob Ramsay[2], Trevor Benson[3], Slawomir Sujecki[3], Nabil Abdel-Moneim[3], Zhuoqi Tang[3], David Furniss[3], Angela Seddon[3], Ole Bang[1,4]

[1] DTU Fotonik, Department of Photonics Engineering, Technical University of Denmark, DK-2800 Kgs. Lyngby, Denmark.
[2] Department of Chemistry, Aarhus University, DK-8000 Aarhus C, Denmark.
[3] George Green Institute for Electromagnetics Research, Faculty of Engineering, University Park, University of Nottingham, Nottingham NG7 2RD, United Kingdom.
[4] NKT Photonics A/S, Blokken 84, DK-3460 Birkerød, Denmark.

*e-mail: chru@fotonik.dtu.dk

I. Nonlinear pulse propagation simulations

The discussion of the pulse propagation dynamics in the highly-nonlinear fibre was supported by numerical simulations. Supercontinuum generation (SCG) was modelled using the generalized nonlinear Schrödinger equation (GNLSE), which is a standard framework used for this type of modelling where only a single spatially invariant mode and single polarisation is considered. The GNLSE was rewritten into an interaction picture formulation and integrated using the 4th order Runge-Kutta integration method with adaptive step-size, based on the Local Error Method algorithm[1]. The spectral and temporal windows were composed of 2^{16} bins with the spectral window spanning from 1-30μm yielding a temporal resolution dt=3.6fs and spectral resolution df=4.2042GHz. A series of peak powers were chosen in the simulations in order to best match the simulated SC spectra to the short and long wavelength edges of the experimental spectra. The linear propagation operator in the simulations was based on the calculated fibre dispersion using COMSOL Multiphysics together with the measured fibre loss of an intermediate 296μm core diameter fibre. The loss was only measured out to 12.5μm, where it is about 25dB/m. In the simulations we artificially set the loss to 1000dB/m above 12.5μm to avoid overloading the spectral window. The nonlinear operator was given by the Kerr coefficient from slusher *et al.*[2] and Raman gain from Ung & Skorobogatiy[3].

Ia. Normal dispersion 4.5μm pump case

The dynamics and the qualitative dependence on the peak pump power of the 4.5μm pump case is remarkably well reproduced by modelling of the FM alone, as seen in Fig. A. We believe this is because the dynamics are initially determined by self-phase modulation (SPM). Even after the SPM generated light crosses the zero-dispersion wavelength (ZDW) at ~5.83μm, the simulations produce the heavily modulated spectrum consistent with soliton dynamics. The peak power used in the simulations was reduced by a factor of ~5 in order to reproduce the same features as seen in the experiment. This factor we attribute to a combination of measurement uncertainty, a factor two power loss due to coupling to the orthogonal polarisation, and further power loss from coupling to HOMs.

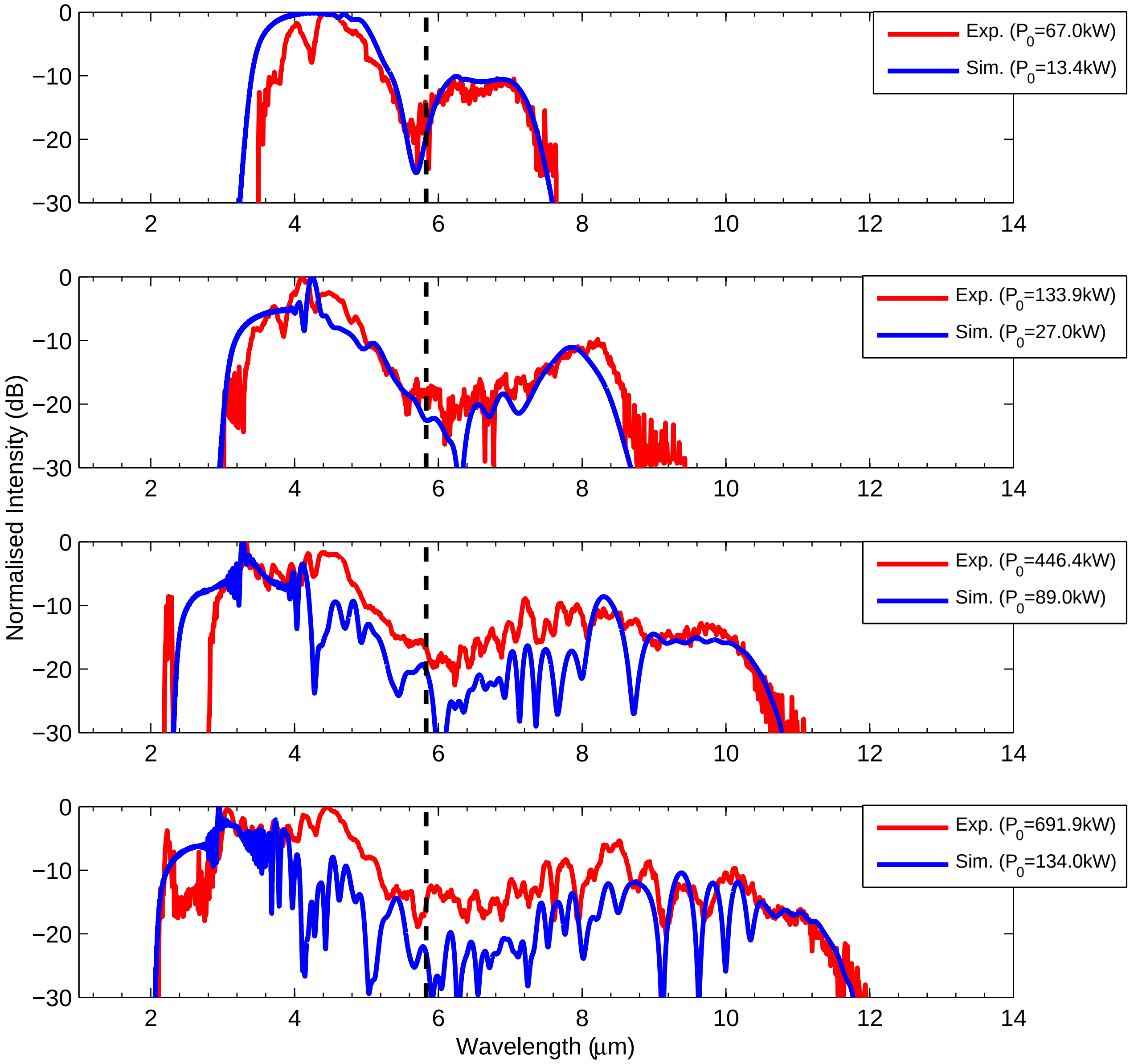

Figure A | Comparison between experimental (red solid) and simulated (blue solid) SCG in the 4.5µm pump case for varying input peak power, together with the ZDW of the fibre (black dashed). The simulations were able to reproduce many of the same features present in the experimental spectra by reducing the simulated input peak power by a factor of ~5, which then accounts for measurement uncertainty, loss of power to the orthogonal polarisation and HOMs. However, the short-wavelength SPM edge was consistently shorter than what was observed experimentally, which may be due to a much higher loss of the test fibre at 2.9µm compared to the large-core fibre used for loss measurements.

Ib. Anomalous dispersion 6.3µm pump case

The 6.3µm pump simulations were able to reproduce some of the same features present in the experimental spectra at low input power, such as the formation of what appears to be dispersive waves (DW) in the normal dispersion regime, as can be seen in Fig. B. The simulated input peak power was reduced by a factor of ~17.5 in order to obtain qualitative correlation with the experimental data, and the high factor may be due to the fact that in our experiment a large part of the light is present around the pump wavelength, where the simulations predict that a large part of the light will be shifted away. This discrepancy is attributed partly to the excitation of HOMs, which tend to cause little broadening and thus increase the signal around the pump as demonstrated by Poletti *et al.*[4]. Only experimental data for broadening below 12.5μm was compared with simulations because of the artificial loss edge.

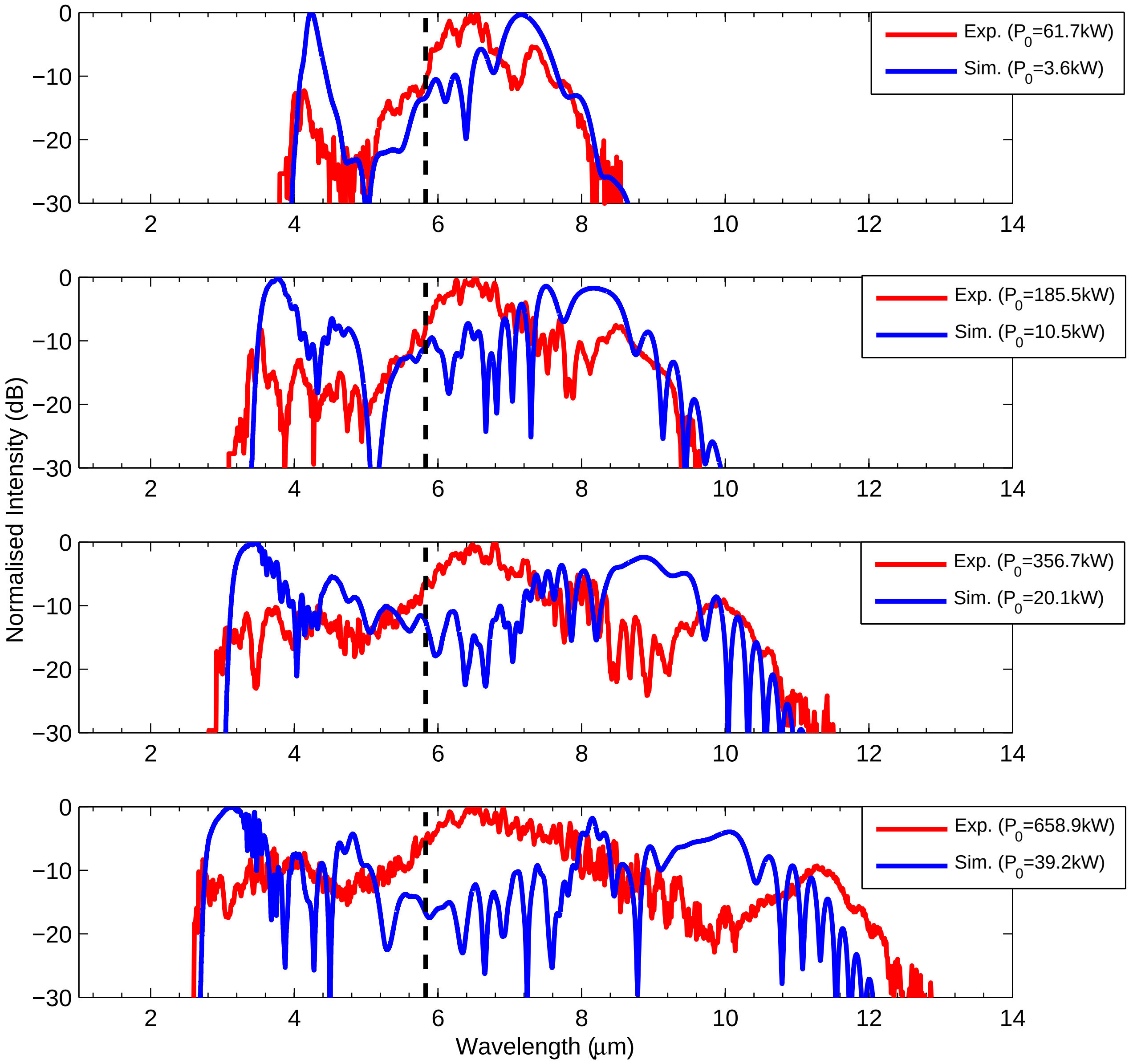

Figure B | Comparison between experimental and simulated SCG for the 6.3μm pump case for varying input peak power, together with the ZDW of the fibre (black dashed). The simulations were able to reproduce some of the same features present in the experimental spectra at low input power by reducing the simulated input peak power by a factor of ~17.5. The high factor may be due to the fact that in our experiment a large part of the light is present around the pump wavelength, where the simulations predict that almost all of the light will be shifted away. This may be caused by the excitation of HOMs, which tend to cause little broadening and thus increase the signal around the pump.

II. Data post processing

The final data presented in the manuscript is the result of careful data processing involving calibration correction, data stitching and image processing. This section provides an overview of the data processing performed on the presented data.

IIa. Blackbody detector calibration

A full blackbody calibration was performed using a 1323K cavity blackbody source from Infrared Systems Development. Fig. C shows the measured blackbody spectrum compared to the theoretical blackbody radiation curve given by Planck's radiation formula[5]:

$$S_\lambda = \frac{8\pi hc}{\lambda^5} \frac{1}{\exp\left(\frac{hc}{\lambda kT}\right) - 1}$$

where S_λ is the energy per unit volume per unit wavelength, h is Plancks constant, k is the Boltzmann constant and T is the temperature of the blackbody. A series of long-pass filteres were used as order sorting filters, and the transmission of each filter was compensated by measuring the transmission spectrum over the respective wavelength range using an FTIR spectrometer.

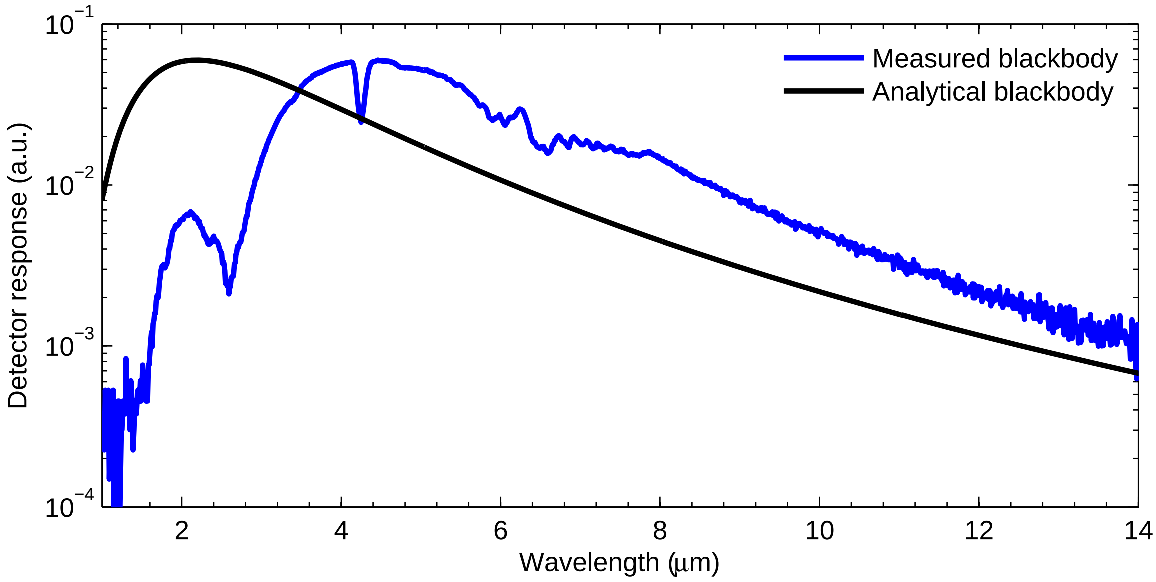

Figure C | Comparison between the theoretical and measured blackbody radiation spectrum. From the discrepancy between measured and analytical blackbody radiation a calibration function for the detection system was derived.

From the measured blackbody spectrum it is evident that the detection system efficiency was reduced substantially below 2µm, vanishing at around 1.5µm. Furthermore, the measured spectrum was affected by absorption in the air from H_2O and CO_2, which enabled us to also compensate for this in the measurement data. A similar measurement was performed for the InGaAs array detector to also calibrate the short-wavelength edge.

IIb. Data stitching and data correction

Fig. D illustrates how the raw data collected from the MCT detector with different long-pass filters (blue, green and red) was stitched together at 5μm and 8μm by compensating for the different transmission of the long-pass filters. The long-pass filter transmission spectra was measured using an FTIR spectrometer. The short-wavelength edge data collected by the InGaAs array (black) was stitched on to the blue curve by matching the response values at ~2μm. The spectrum was subsequently calibrated by applying a calibration function determined from blackbody calibration of the two detectors.

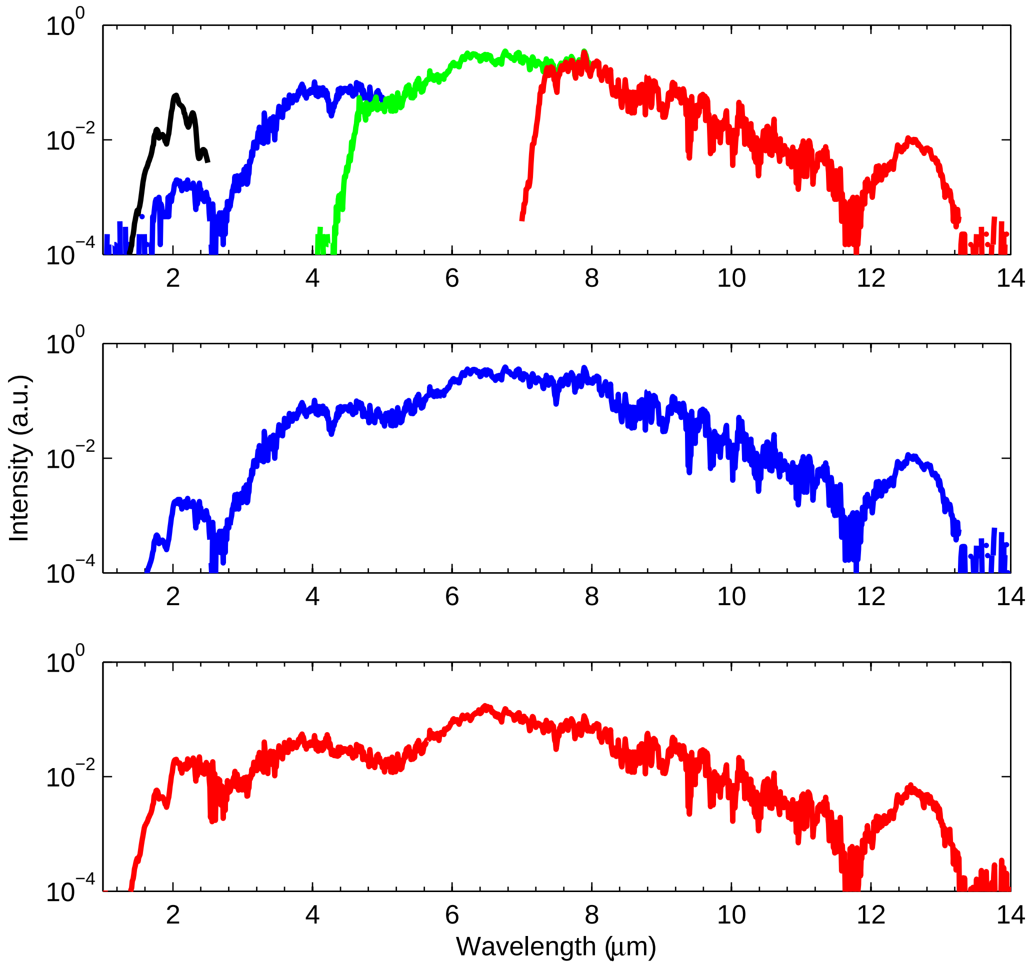

Figure D | Spectral data processing. Example of how the raw data from the 6.3μm pump experiment (top) was stitched together (middle) and corrected using the calibration data of the two detectors to obtain the actual shape of the spectrum (bottom).

IIc. Image processing

The fibre output beam profiles presented in Figs. 4.c and 5.c+d of the manuscript depict the raw image data, while the beam profile of Fig. 4.d has been subjected to noise removal and average filtering. This was performed to improve the image quality, which was heavily reduced due to low detected signal-to-noise ratio, which was a consequence of placing the 7.3μm long-pass filter in front. The result of image processing is displayed in Fig. E.

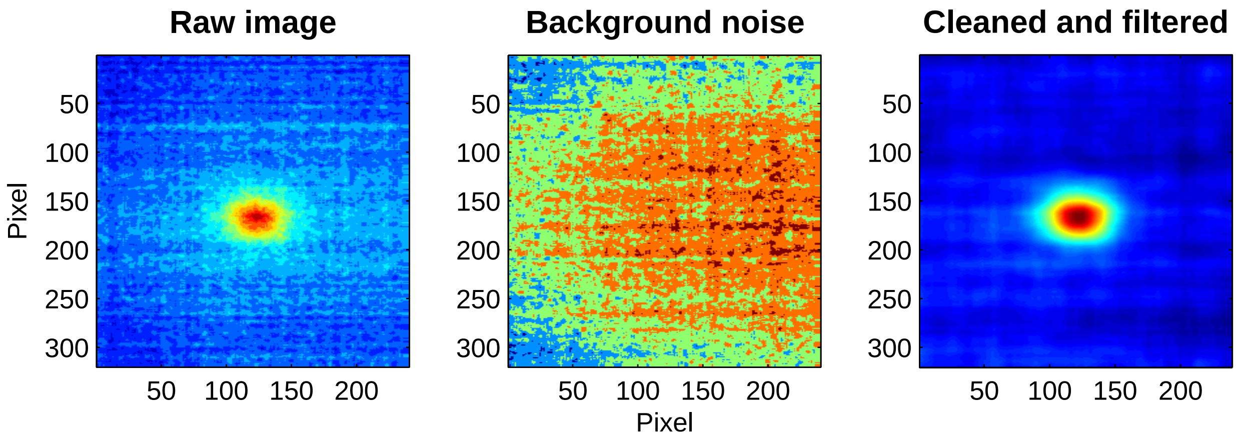

Figure E | Beam profile image processing. Process of taking the raw data image (left), subtracting the background noise (middle) and average filtering to obtain a more clear image (right).

III. Spectral stability

The stability of the output spectrum can be described by the shot-to-shot variations in both intensity, bandwidth and distinct features. In order to quantify the stability of our spectrum we measured the long-wavelength edge for different degrees of averaging in both the 4.5μm and 6.3μm cases. The low repetition rate of 1kHz (1 pulse per ms) allowed us to perform single-shot sampling, which was then compared to the same measurement with averaging over 100 samples, as shown in Fig. F. A box-car integration time of 2.494μs and monochromator wavelength sampling resolution of 10nm was used. This means that a single-shot spectrum from 7-12μm consist of 500 pulses, and as can be seen from Fig. F, the same features and bandwidth is obtained for the 100 averaging case for 50,000 pulses.

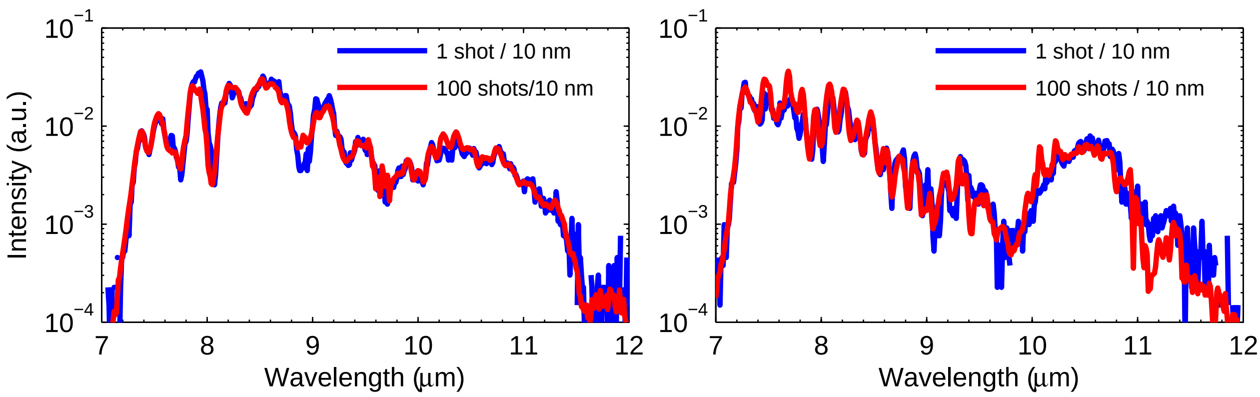

Figure F | Shot-to-shot stability analysis. Comparison between single-shot per 10nm spectrum and averaging over 100 pulses per 10nm in the 4.5μm (left) and 6.3μm (right) pump cases, which shows that the spectrum is quite stable considering the free-space coupled nature of the set-up.

IV. Dispersion measurements and analysis

The dispersion of the fundamental mode of the fibre was measured by means of spectral-domain interferometry using a ZBLAN supercontinuum source. This technique is described in details in the paper by Hlubina[6], but briefly described the set-up consisted of a balanced Mach-Zehnder interferometer wherein a 165mm test fibre was placed in one arm and the other free-space arm was varied in length by a translation stage. Matching the optical path delay of the two arms gives rise to a spectral beating, a so called fringe pattern, as can be seen in Fig. G.

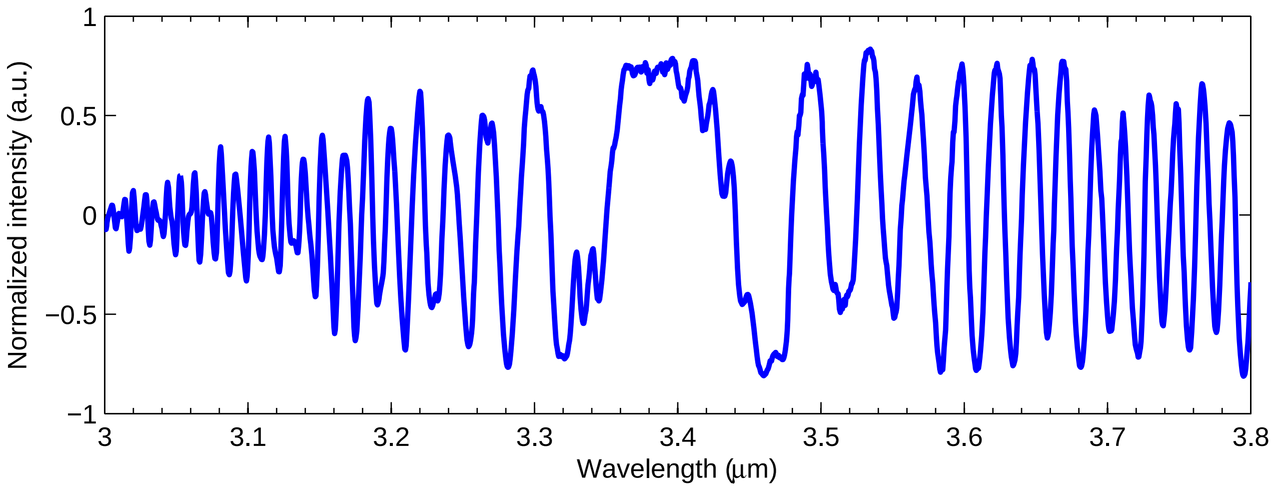

Figure G | Fringe spectrum from spectral beating between the test and reference arm of the interferometer. The fringe spacing becomes larger as the wavelength approaches the equalization wavelength ~3.4μm, which is the wavelength at which the delay between the two arms is equal. Around this wavelength a higher-order beating can also be seen, which is the result of beating with higher-order modes.

From the observed fringe pattern, one may identify a symmetry point around 3.4μm, the phase equalisation wavelength, where the delay of the fundamental mode of the two arms is matched. By fitting the position of fringe peaks and valleys to a modified Cauchy dispersion formula the dispersion of the fundamental mode can be extracted. The measured dispersion of the fundamental mode is presented in Fig. H, which represents the average over several measurements with varying equalisation wavelengths.

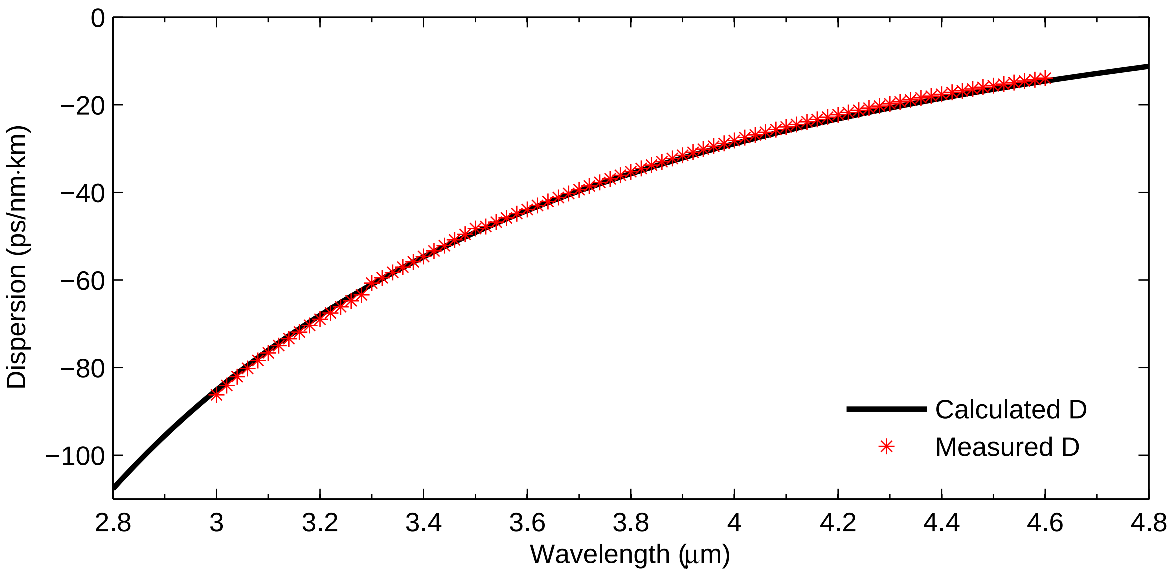

Figure H | Comparison between the calculated (solid) and measured (asterix) dispersion of the fundamental mode of the fibre. The measured dispersion was found to be within ±1 ps/nm km of the calculated dispersion.

As can be seen from the fringe pattern in Fig. G, especially around the phase equalisation wavelength, a higher-order modulation is present, which through a sliding-window Fourier transform analysis was identified as a higher-order mode (HOM) beating. The interferograms obtained from the sliding-window Fourier transform is presented in Fig. I.

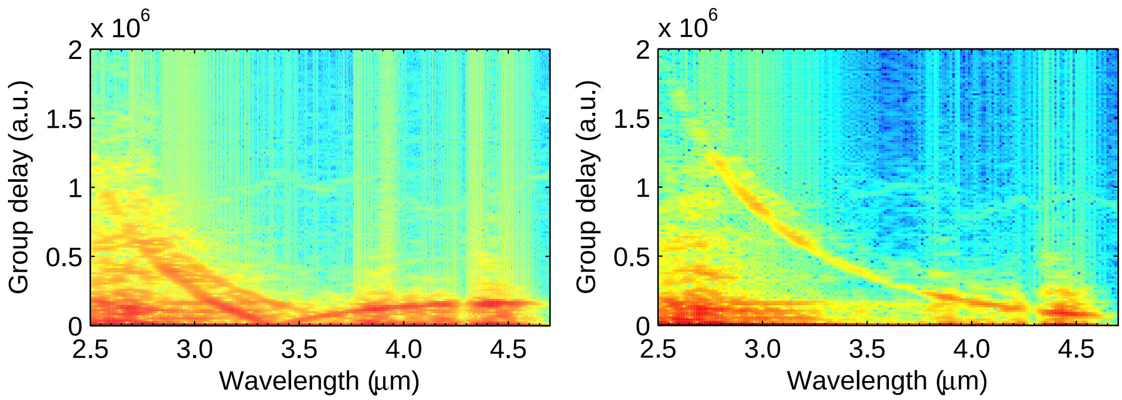

Figure I | Spectrograms generated from sliding-window Fourier transformation. Comparison between the observation of two distinct modes with different group delay curves (left) and only a single distinct mode (right).

The curve inversion seen at ~3.4µm in the left panel of Fig. I corresponds to the phase equalisation point of Fig. G, and since it is the dominant curve it is assumed to be the fundamental mode. When comparing to the modelled fibre delay in Fig. J a strong resemblance to the LP01 and LP11 can be seen. The presence of only one HOM in the spectrogram signifies that there is negligible coupling, scattering or beating with even higher orders of modes. In many cases we only observed the FM, as can be seen in Fig. I.b.

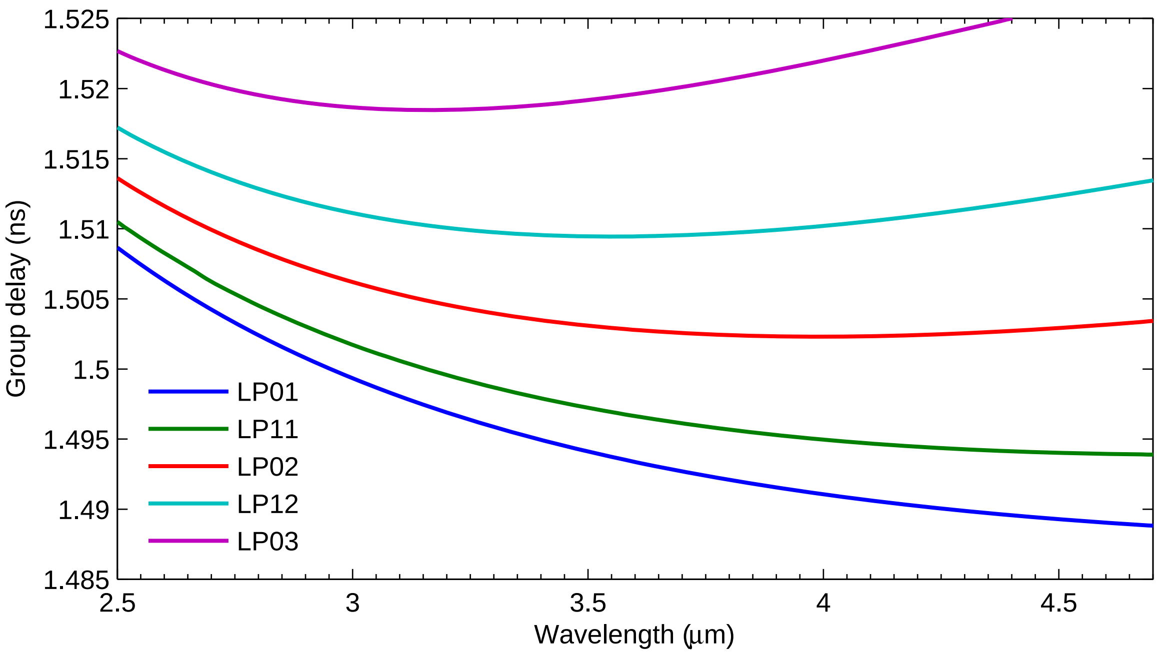

Figure J | Modelled fibre delay for the five predominant modes. The LP01 and LP11 modes are very close in terms of group delay, similar to what was observed experimentally in the left panel of Figure I.

References

1. Heidt, A. M. Efficient Adaptive Step Size Method for the Simulation of Supercontinuum Generation in Optical Fibers. *J. Light. Technol.*. **27**, 3984–3991 (2009).

2. Slusher, R. E. et al. Large Raman gain and nonlinear phase shifts in high-purity As2Se3 chalcogenide fibers. *J. Opt. Soc. Am.* **21**, 1146–1155 (2004).

3. Ung, B. & Skorobogatiy, M. Chalcogenide microporous fibers for linear and nonlinear applications in the mid-infrared, *Opt. Express* **18**, 8647–8659 (2010).

4. Poletti, F. & Horak, P. Dynamics of femtosecond supercontinuum generation in multimode fibers. *Opt. Express* **17**, 11301–11312 (2009).

5. Siegel, R. & Siegel, Howell, J. Thermal radiation heat transfer, (Taylor & Francis, 2002).

6. Hlubina, P. Spectral interferometry-based chromatic dispersion measurement of fibre including the zero-dispersion wavelength. *J. Eur. Opt. Soc. Rapid Pub.* **7***,* 12017 (2012).